Nanoscale

ROYAL SOCIETY OF CHEMISTRY

PAPER

View Article Online
View Journal | View Issue

Cite this: *Nanoscale*, 2025, **17**, 21070

A close-space sublimation approach to tungsten oxide and sulfide nanostructure formation

Hao Yu, [a] Jinfeng Yang,[a] Bernhard Fickl, [b] Shaoliang Guan,[a] Oliver J. Burton, [a] Gwenhivir Wyatt-Moon,[a] Andrew Flewitt, [a] Bernhard C. Bayer [b] and Stephan Hofmann *[a]

We present a highly resource-efficient Close-Space Sublimation (CSS) approach, along with versatile one-step and two-step process designs, for the controlled synthesis of a wide range of tungsten (sub)oxide (WO_{3-x}) and tungsten disulfide (WS_2) nanostructures. By applying a simple sublimation model and leveraging graded CSS flux profiles in conjunction with *operando* experimentation, we accelerate process discovery and establish CSS flux and substrate temperature as key parameters governing nanostructural formation. Our CSS methodology enables the synthesis of W (sub)oxide structures within process times of less than 10 minutes, a significant improvement over the hour-long durations typically required in conventional hot-wall furnace systems. We elucidate how nanostructural control in the CSS approach arises from the kinetic interplay between the tungsten oxide sublimation flux and the rate of oxygen depletion in the deposited layers, thereby facilitating the formation of distinct W suboxide templates with varied structural motifs. These findings highlight CSS as a highly promising alternative to conventional powder-furnace chemical vapour deposition, offering superior efficiency, precise structural control, scalability, and adaptable process designs tailored to applications spanning photo-/electro-catalysis, photovoltaics, sensors, and highly integrated optoelectronic devices.

Received 10th April 2025,
Accepted 5th August 2025

DOI: 10.1039/d5nr01458a

rsc.li/nanoscale

Introduction

Nanostructured tungsten (sub)oxides and sulfides have an application horizon ranging from photo-/electro-catalysis[1] and photovoltaics[2] to sensors,[3,4] superconductors,[5] integrated optoelectronics and neuromorphic computing.[6–9] This reflects significant demand for tailored, scalable synthesis approaches that are efficient and enable high structural control.[10] The development of versatile, high-throughput synthesis methods is also essential to advance the underpinning fundamental understanding, particularly regarding dimensional and nanostructural control. Tungsten (sub)oxides and sulfides in this context present highly interesting model systems connecting anisotropic filamentary 1D nanowire/whisker growth and nanotube and 2D mono- and few-layer formation.[11–13] Both 1D WS_2 nanotubes (NTs) and 2D WS_2 layers can form *via* intermediary tungsten suboxides, highlighting the interconnected nature of these materials and the wide synthesis parameter space.[14,15]

Conventional chemical vapor deposition (CVD) methods, particularly hot-wall furnace-based approaches, are widely employed for WS_2 nanostructure synthesis using powder precursors. The fabrication of WS_2 NTs typically follows a two-step CVD route, wherein tungsten suboxide nanowires are first synthesized and subsequently sulfurized.[14,16–20] For 2D WS_2 films, a one-step CVD process is commonly used, with sulfur and metal oxide powders positioned at different locations within the furnace – typically with the oxide precursor placed either close to or directly beneath the substrate.[15,21] While being simple and versatile, such powder-based CVD approaches pose significant challenges. Precise control over the reaction environment is difficult due to the highly position-dependent gas composition linked to flux/reaction time in the hot zone environment, further complicated by many possible contamination effects including those from furnace walls (also negatively affecting batch-to-batch reproducibility). They are inherently resource-inefficient, both in terms of precursors and energy, with large reactor sizes and associated large thermal masses resulting in typical high temperature process durations exceeding 5 h, and with inherent inhomogeneities leading to only a tiny fraction of volume being utilised as the reaction zone. These factors have held back both fundamental understanding and scalable manufacturing.

Close-space sublimation (CSS) offers a compelling alternative, combining simplicity, high throughput, and resource efficiency. While CSS has been extensively employed in thin-

[a]*Department of Engineering, University of Cambridge, JJ Thomson Avenue, CB3 0FA Cambridge, UK. E-mail: sh315@cam.ac.uk*
[b]*Institute of Materials Chemistry, Technische Universität Wien, Vienna, Austria*

film growth for CdTe and related alloys in photovoltaic and optical detector applications,[22,23] recent work has demonstrated its applicability to a wider range of materials, including metals,[24] hybrid perovskites, and oxides.[25] Moreover, CSS can be effectively integrated with CVD-type reactions, such as metal oxide growth followed by exposure to a chalcogen precursor.[26] The ability to deconstruct complex reaction scenarios is important to foster an advanced understanding, including *via in situ*/*operando* experimentation.[27]

In this study, we explore a CSS-based strategy for synthesizing tungsten (sub)oxide and sulfide nanostructures, motivated not only by its resource efficiency but also by the ability to achieve structural control through confined, high-flux deposition. Using a sputtered WO_3 thin film as a precursor and a sublimation-limited model to estimate deposition flux, we systematically explore structural control on a SiO_2/Si target substrate *via* sequential 2-step and combined 1-step process designs with a sulphur precursor exposure, using gaseous dimethyl disulfide (DMDS) or solid S evaporation. We exploit the ability to create graded CSS flux profiles to accelerate parameter space screening. We show that by tuning temperature and sublimation flux a wide range of different W suboxides and different nanostructuring can be reproducibly and highly efficiently achieved by CSS. We utilise *operando* scanning electron microscopy (OSEM) to show how as-grown W suboxides can underdo significant further structural transformations upon subsequent sulfidation. We demonstrate that a 1-step approach, where tungsten oxide CSS and DMDS exposure occur simultaneously, enables the rapid (<10 min) fabrication of WS_2-coated tungsten suboxide nanowires, with a diameter of approx. 20 nm and lengths around 2 μm. We further show that 2-step processes with S exposures subsequently carried out in a CVD furnace allow us to access the full reported range of W sulfide nanostructures. Our results motivate CSS as a highly promising alternative to conventional powder-furnace CVD, offering superior efficiency, scalability, and control. Our findings position CSS as an advanced versatile platform for both accelerated combinatorial process discovery and the scalable, efficient manufacturing of complex nanostructures.

Results

Sublimation model

Fig. 1a and b present a cross-sectional schematic and a top-view of the CSS setup, respectively. The source and substrate are separated by a sapphire spacer with a fixed thickness of h = 0.5 mm. We assume tungsten trioxide sublimation to be congruent under our range of conditions, with the vapour consisting mainly of W_3O_9 and W_4O_{12}.[28–31] We estimate the mean free path λ of the primary W_3O_9 species using the expression:[32]

$$\lambda = \frac{k_B T}{\sqrt{2}\pi d^2 P} \quad (1)$$

where T is the source temperature (T_{source} = 750–950 °C), k_B is the Boltzmann constant, d represents the molecular diameter

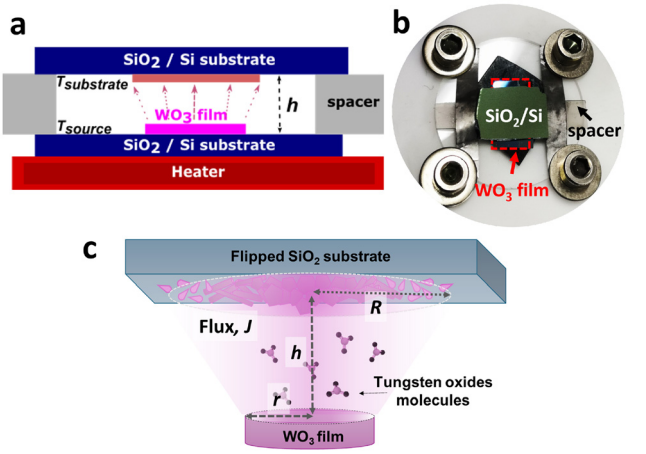

Fig. 1 (a) Schematic cross-sectional view of the close-space sublimation set-up, where the height between two plates is h, temperature of the top substrate is $T_{substrate}$, temperature of the WO_3 source is T_{source}; (b) top-view image of the set-up; (c) simplified model of the close-space sublimation, where R is the radius of the deposited region on the top substrate and r is the radius of the pre-deposited film at the bottom; monomers of $(WO_3)_n$ gas molecules are drawn here for simplicity of illustration.

of W_3O_9 (assumed to be 1 nm), and P is the chamber pressure. For a typical operating pressure of 0.02 mbar, the Knudsen number can be estimated as $K_n = \frac{\lambda}{h} > 1$. We can thus assume a molecular flow regime and estimate the net W_3O_9 flux $J_{net}(R)$ reaching the substrate surface as:[25]

$$J_{net}(R) = \frac{n_{max}}{2}\log\left(\frac{1}{2} + \frac{r^2}{2h^2} - \frac{R^2}{2h^2} + \sqrt{\frac{1}{4} + \frac{(R^2 - r^2)^2}{4h^4} + \frac{(R^2 + r^2)}{2h^2}}\right) - n_{counter} \quad (2)$$

where R and r are defined in Fig. 1c, n_{max} represents the flux determined by the Hertz–Knudsen equation,[32] and $n_{counter}$ accounts for re-emission from the substrate due to its high temperature ($T_{substrate}$). In this model system, net deposition of a film requires a negative temperature difference, *i.e.*, $T_{source} > T_{substrate}$.

This model provides insights into the resulting deposition profiles. Previous studies demonstrated that uniform film deposition can be achieved by selecting $r > R$.[25] However, in this work, our initial focus is on process discovery by utilizing graded flux and thickness profiles, and we therefore predominantly select $r < R$. We employed CSS from sputtered and patterned WO_{3-x} films to fabricate tungsten (sub)oxide template structures for subsequent or simultaneous sulfidation. We note that the flux estimation above is idealised, in particular as W suboxides are known to have different volatility.[28,33,34] In contrast to the CSS thin film literature where a primary aim is to control film thickness, our focus here is to explore how CSS can enable control of the nanostructure of the as-grown W (sub)oxide. This is motivated by literature using conventional CVD reactors to grow a range of 1D and 2D WS_2 nanomaterials,

whereby W suboxides act as structure-defining common templates.[15]

WO_3 morphologies from CSS in an inert environment

We employed a 1 mm × 1 mm square-patterned WO_3 precursor film ($r \approx 1$ mm) and performed CSS at 0.02 mbar of Ar, as illustrated in the process schematic (Fig. S1). Comparable growth results are obtained for CSS carried out under base pressure ($\approx 1 \times 10^{-6}$ mbar, see Fig. S2), which is consistent with our model assumptions. The use of Ar pressure primarily ensures consistency for later experiments involving reactive gases at the same pressures.

Fig. 2a presents an optical image of the CSS-deposited tungsten (sub)oxide on a SiO_2/Si wafer substrate under white light illumination. A distinct color transition from pink to yellow is observed as a function of radial distance (R) from the centre. The variation of colour depending on the detailed oxidation state is well known for tungsten oxides,[35–37] but as here also the nanostructuring will play a significant role, we use colour only to highlight the level of sample heterogeneities. Using eqn (2), we estimate the underlying tungsten oxide flux profile (Fig. 2b). SEM characterization across deposition locations 1–4 (Fig. 2c) reveals distinct morphological variations. These results represent the maximum flux and do not account for temperature ramp effects. Preliminary investigations indicate that varying the temperature ramp rate does not significantly alter the dominant deposition morphology within the deposition time range of 5–10 min (see Fig. S1).

At the central deposition spot (spot 1, R = 0.1 mm), bulky W oxide facets (~50 nm wide) are observed, along with nanorods (~20 nm wide, >200 nm long) distributed on the surface. Moving outward to spot 2 (R = 0.8 mm), W oxide flakes are interspersed with nanowhiskers (~15 nm wide, ~150 nm long). At spot 3 (R = 2 mm), high-aspect-ratio W oxide nanowires/nanowhiskers dominate, with an average length of 350 nm and an average width of 15 nm. At the outermost deposition region (spot 4, R = 3.5 mm), fine nanowhiskers of W oxide are structurally dominant, measuring < 50 nm in length and 10 nm in width.

X-ray photoelectron spectroscopy (XPS) analysis of the W 4f core-level spectrum provides insight into the composition of W oxide across deposition locations 1–4 (Fig. 2d). The W $4f_{5/2}$ peak at a binding energy of 38.2 eV and the W $4f_{7/2}$ peak at 36.1 eV appear in both the original WO_3 precursor and the deposited regions. However, the peaks exhibit progressive broadening as the scan position shifts from the centre (position 1) toward the edge (position 4). In order to quantify the oxidation state variations, valence component curve fitting was performed following the methodology outlined in a previous study.[38] The XPS curve from position 1 to 4 shows an increase of shoulder peaks at 37.0 eV and 34.9 eV. The results indicate a progressive increase in the relative area of the W^{5+} component from position 1 to position 4, suggesting a reduction in the oxidation state of WO_{3-x} from the centre to the periphery of the CSS deposition region. By comparing the area ratio of W^{6+} and W^{5+} valencies, we calculated the average W : O ratio from

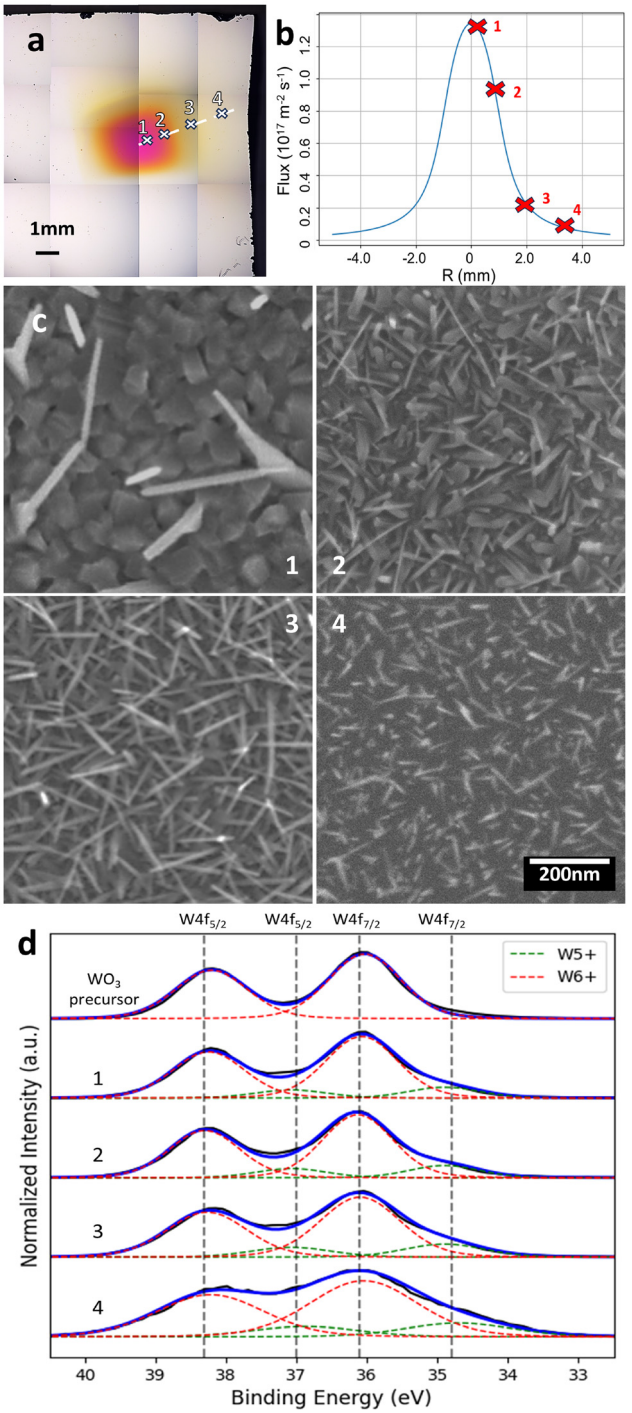

Fig. 2 (a) Stitched OM image of WO_{3-x} deposition after heating at P_{Ar} = 0.02 mbar and $T_{substrate}$ = 760 °C for 10 minutes in the CSS set-up, where sample spots 1 to 4 are located at the following distances from the centre: R_1 = 0.2 mm, R_2 = 0.8 mm, R_3 = 2 mm, and R_4 = 3.5 mm; (b) flux profile calculated corresponding to locations 1 to 4, with the calculated flux values being 1.3×10^{17} m^{-2} s^{-1}, 9.8×10^{16} m^{-2} s^{-1}, 2.2×10^{16} m^{-2} s^{-1}, and 6.9×10^{15} m^{-2} s^{-1}, respectively; (c) SEM images at locations 1 to 4; (d) W^{4f} core level XPS spectra of the WO_3 precursor and deposited WO_{3-x} samples at positions 1 to 4, respectively.

position 1 to 4 to be 2.92, 2.90, 2.81 and 2.72. The variation of XPS signatures and peak evolution is reminiscent of previous literature that reported the thermal (surface) reduction of WO_3 films under vacuum.[39]

Our data demonstrate that the imposed flux gradients lead to the formation of distinct nanostructured W oxide, rather than a continuous thin film with varying thickness. Additionally, temperature ramp variations (see Fig. S1) exhibit minimal impact on the resulting structural morphology. Fig. S2 provides a comparative SEM characterization of a CSS deposition performed at half the deposition time under otherwise identical conditions. The W oxide motifs observed across spots 1–4 (Fig. 2) are consistent with those in Fig. S2, albeit with lower density and/or reduced dimensions.

Importantly, there is no formation of nanorods on the WO_3 precursor film held at T_{source}, as confirmed in Fig. S3. Instead, the source film becomes increasingly porous over time. Under the given CSS conditions, we find that a sufficient reservoir of the source material remains after a complete deposition cycle, indicating that the sublimation flux is sustained throughout the entire process (see Fig. S1).

Operando sulfidation and WS_2 formation

We explore a two-step process in which nano-structured W oxide deposited *via* CSS is subsequently transferred to a separate reactor and exposed to a gaseous dimethyl disulfide (DMDS) precursor to induce WS_2 overlayer growth. We employed an *operando* scanning electron microscopy (SEM) setup, equipped with a high-temperature stage and a localized DMDS gas injector (see the Experimental methods section), to monitor structural transformations during the sulfidation reaction in real-time.[40] We used such *operando* sulfidation to gain fundamental process insights, and hence achieve effective *ex situ* parameter screening and CSS process development.

Fig. 3a presents a representative sequence of *operando* SEM images recorded during DMDS injection at elevated temperature. The CSS-deposited W oxide was heated to 700 °C under high vacuum ($\approx 10^{-6}$ mbar), and the local DMDS pressure was estimated to be of the order of 0.02 mbar based on Test-Particle Monte Carlo (TPMC) simulations.[40] The image sequence reveals the axial elongation of the initial rod-like W oxide structures. This growth ceases after approximately 550 s, at which point the high-aspect-ratio structures reach lengths exceeding 1 μm. Post-sulfidation Raman spectroscopy analysis (Fig. 3b) confirms the formation of WS_2, as evidenced by the presence of characteristic vibrational modes. These include the 2LA(M) mode at 345.0 cm^{-1}, the $E_{2g}{}^1(\Gamma)$ mode at 355.0 cm^{-1}, the $A_{1g}(\Gamma)$ mode at 418.0 cm^{-1}, and the $B_{1u}(\Gamma)$ mode at 413.8 cm^{-1}.

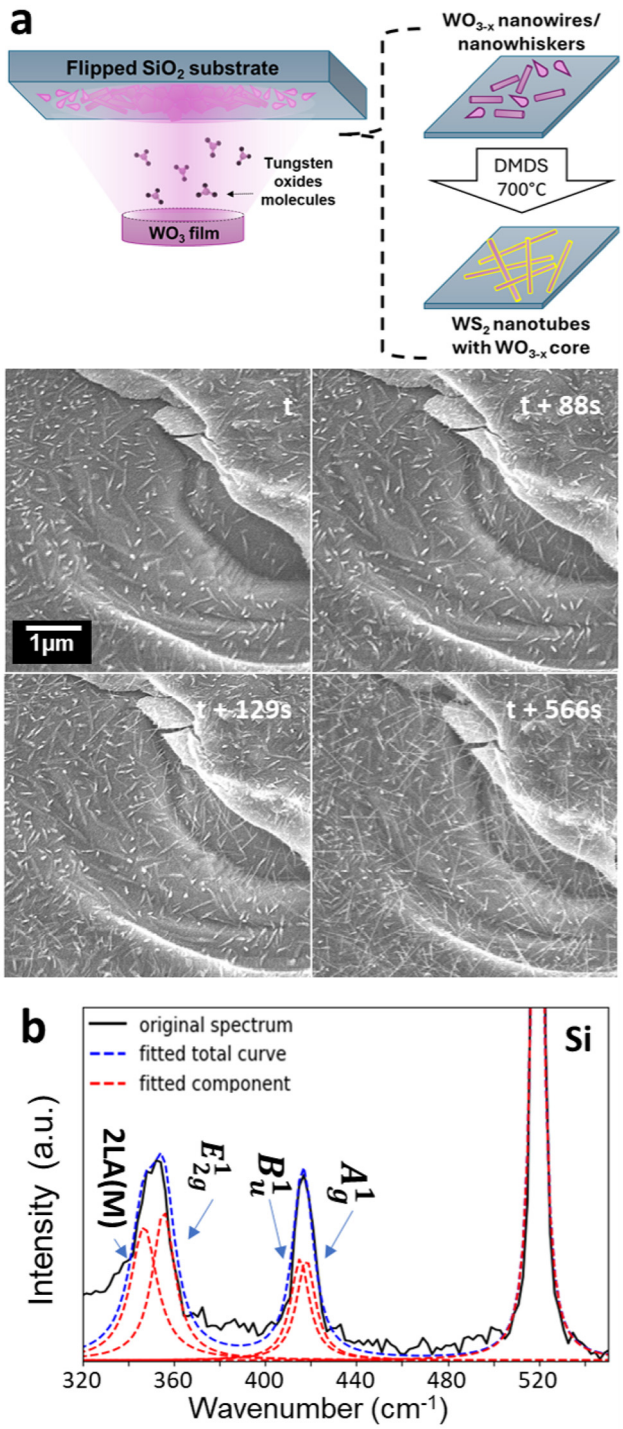

Fig. 3 (a) Schematic of the *operando* sulfidation process and SEM image series during DMDS exposure at 700 °C for t to t + 300 s; (b) Raman spectrum and fitted component curves for the exposure site. Peaks of 2LA(M) were found at 345.0 cm^{-1}, $E_{2g}{}^1(\Gamma)$ mode at 355.0 cm^{-1}, $A_{1g}(\Gamma)$ mode at 420.0 cm^{-1}, and $B_{1u}(\Gamma)$ mode at 413.8 cm^{-1}, respectively.

Single-step CSS in the DMDS environment

We employed a square-patterned WO_3 precursor film under conditions analogous to those in Fig. 2, but performed the CSS process under 0.02 mbar of DMDS (see the Experimental methods section). Given that $K_n > 1$ (eqn (1)), we assume that sulfidation in this process remains substrate-bound, thereby excluding significant gas-phase reactions. Eqn (2) implies that the W oxide flux profile remains unchanged. The WO_3 precursor film, maintained at T_{source}, becomes increasingly porous.

However, Raman analysis reveals characteristic WS_2 peaks (E_{2g}^1, A_{1g}) alongside O═W═O stretching modes (Fig. S3), suggesting the formation of a mixed WS_2–WO_{3-x} phase at the source after sulfidation.

Fig. 4a presents an optical image of the post-processed substrate under white light illumination. A distinct colour contrast is observed, transitioning from black to pink to yellow with increasing radial distance (R) from the centre. Raman spectroscopy (Fig. 4b) confirms the presence of WS_2 at spots 1–3, as evidenced by the E_{2g}^1 and A_{1g} modes at 353 cm^{-1} and 420 cm^{-1}, respectively. Additionally, these locations exhibit photoluminescence (PL) exciton peaks at 2.03 eV (Fig. 4c).

Post-process SEM characterization across the deposition profile (Fig. 4d) reveals distinct morphological transitions compared to those of the two-step processes presented in Fig. 2 and 3. At spot 1 (R = 0.2 mm) and spot 2 (R = 0.8 mm), dense, twisted, vertically or slanted-aligned flakes are observed. These microstructures, commonly referred to as "nanoflowers",[41,42] exhibit high light scattering, consistent with the dark appearance of regions with high nanoflower density in the optical image (Fig. 4a). At spot 3 (R = 2 mm), structures with an average diameter of 17 nm and an average length of 350 nm are observed. These structures exhibit a propensity for out-of-plane growth, indicating that they are not purely nanowires or nanowhiskers. At the outermost region (spot 4, R = 3.5 mm), fine nanowhiskers (<50 nm long, 10 nm wide) are found, closely resembling the morphologies observed at spot 4 in Fig. 2c. Higher magnification SEM images of the identified morphologies are shown in Fig. S4.

Fig. 5a summarizes the structural motifs as a function of two key CSS parameters: deposition flux and substrate temperature ($T_{substrate}$). The deposition flux is calculated using eqn (2) and the radial position (R) of a given sample. Since the substrate-to-source gap (h) is fixed in our setup, it is important to recognize that these CSS parameters are interdependent. This interrelationship is reflected in the dashed lines in Fig. 5a, which delineate the accessible deposition conditions within the given experimental setup.

Data collected from over 30 different samples (see Tables S1 and S2 for an overview of CSS conditions) enable the construction of a "zone-map" illustrating the formation of distinct nanostructures. W oxide morphologies are categorized into two primary classes: bulky blocks and nanowhiskers. Similarly, Fig. 5b presents the correlation between $T_{substrate}$ and deposition flux in a single-step CSS setup, identifying three dominant morphologies: nanoflowers, nanowires, and nanowhiskers. At high substrate temperatures (T > 720 °C) and high flux densities (>8 × 10^{16} m^{-2} s^{-1}), nanoflower structures predominate, as illustrated in the representative SEM images (Fig. 5c). Under intermediate flux conditions (2–6 × 10^{16} m^{-2} s^{-1}) and at medium to high substrate temperatures (700–720 °C), nanowire phases become dominant (Fig. 5d).

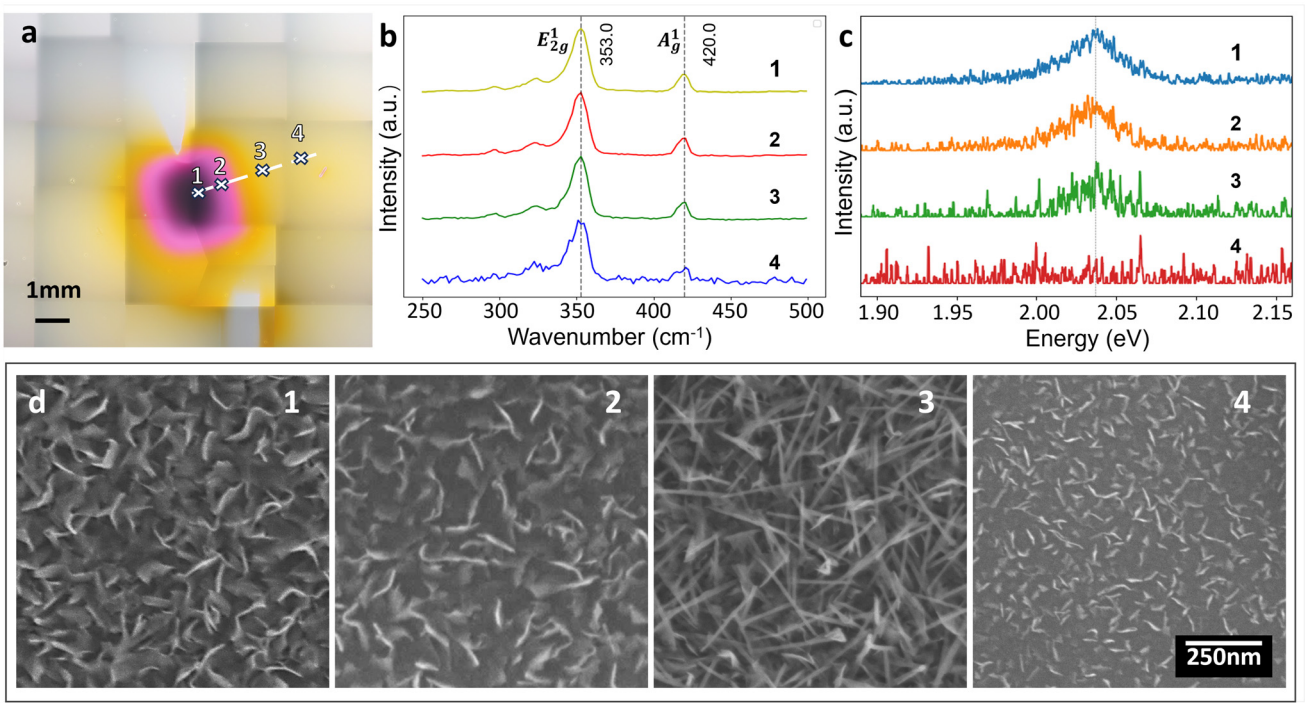

Fig. 4 (a) Stitched OM image of a sample fabricated in the CSS set-up with DMDS gas at a partial pressure of P_{DMDS} = 0.02 mbar, and heated at $T_{substrate}$ = 760 °C for 10 minutes. The precursor at the bottom is patterned to have a 1 mm × 1 mm size, where the sample spots have distances to the centre of deposition as follows: R_1 = 0.2 mm, R_2 = 0.8 mm, R_3 = 2 mm, and R_4 = 3.5 mm; (b) Raman spectrum measured at respective spots 1 to 4 on the sample, where resonance peaks are labelled as E_{2g}^1 and A_g^1 at 353 cm^{-1} and 420 cm^{-1}, respectively; (c) PL spectrum measured at respective spots 1 to 4 on the sample, where the exciton peak is labelled at 2.03 eV; and (d) SEM images of the surface morphology at sites 1 to 4.

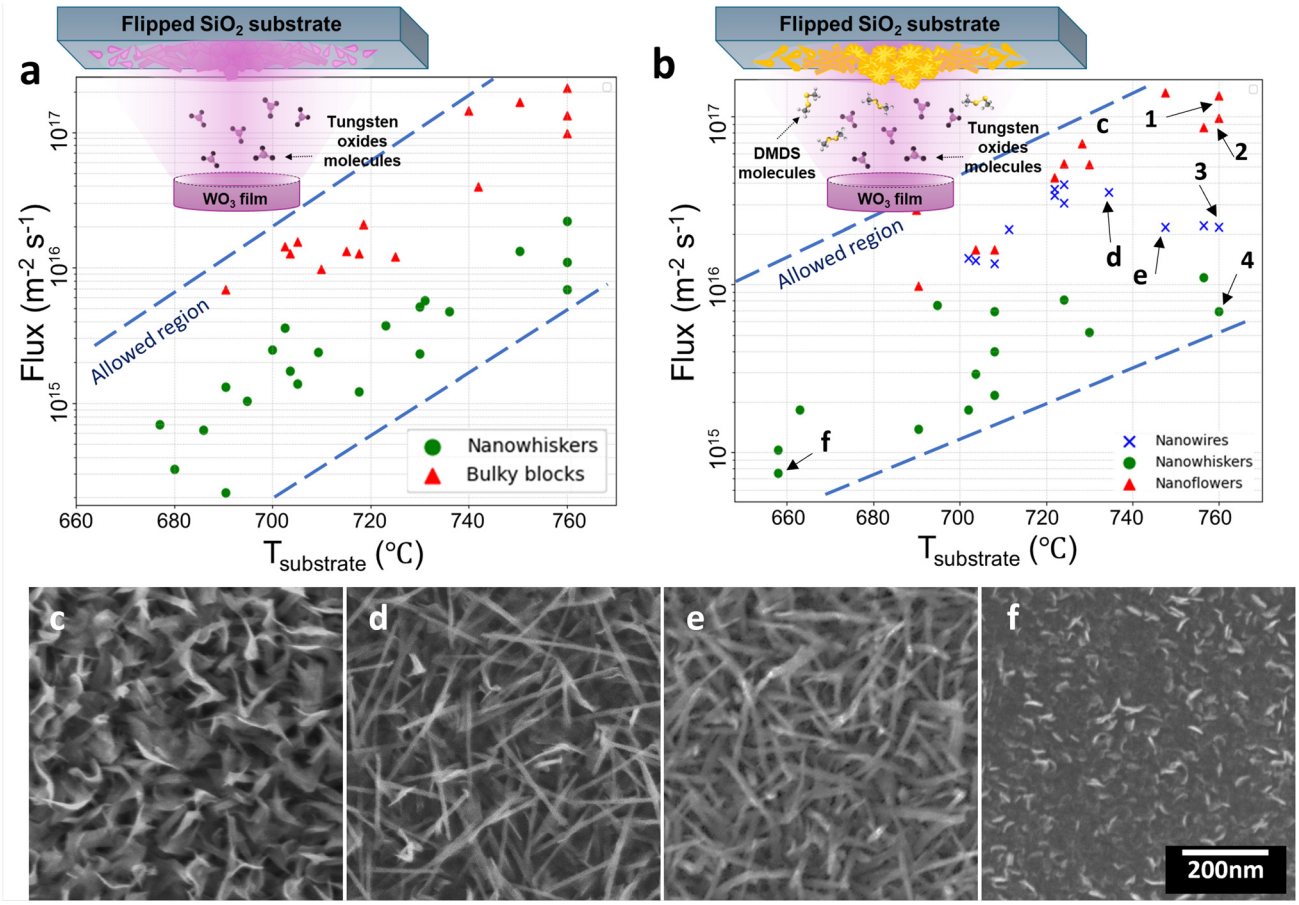

Fig. 5 (a) A schematic of CSS formation of WO_{3-x} and a plot illustrating the two oxide dominant morphologies – bulky blocks and nanowhiskers – on a substrate temperature ($T_{substrate}$) *vs.* flux density diagram. (b) A schematic of the CSS formation of the WS_2–WO_{3-x} heterostructure and a plot illustrating the three dominant morphologies – nanotubes, nanowhiskers, and nanoflowers – on a substrate temperature ($T_{substrate}$) *vs.* flux density diagram. The flux density is plotted on a logarithmic scale on the vertical axis; point 1–4 represents the flux density – $T_{substrate}$ at locations 1 to 4 in Fig. 4. (c–f) SEM images showing morphologies at different substrate temperatures and flux densities: Spot c: $T_{substrate}$ = 756 °C, 8.7 × 10^{16} m^{-2} s^{-1}; Spot d: $T_{substrate}$ = 724 °C, 3.2 × 10^{16} m^{-2} s^{-1}; Spot e: $T_{substrate}$ = 748 °C, 2.2 × 10^{16} m^{-2} s^{-1}; Spot f: $T_{substrate}$ = 658 °C, 7.5 × 10^{14} m^{-2} s^{-1}.

Conversely, at low flux densities (<1 × 10^{16} m^{-2} s^{-1}), nanowhiskers emerge as the dominant morphology, as shown in Fig. 5e and f.

Optimised CSS of WS_2–WO_{3-x} nanostructures

Based on the "zone-map" (Fig. 5b), we focus on conditions that favor nanowire formation in a combined one-step process, specifically a substrate temperature of $T_{substrate}$ = 722 °C and a DMDS pressure of P = 0.02 mbar. To enhance process uniformity and deposition efficiency, we increase r to >1 cm, thereby promoting a more homogeneous flux distribution for W oxide CSS of a uniform structure.

Fig. 6a presents a representative optical microscopy (OM) image of the central substrate region, highlighting uniform sample deposition, as evidenced by the consistent coloration under white light illumination. Corresponding SEM analysis (Fig. 6b) reveals nanowires with high aspect ratios, exhibiting an average diameter of approximately 13 nm and lengths extending up to 2 μm.

Raman spectroscopy and fitted component curves (Fig. 6e) confirm the presence of WS_2, with characteristic peaks for the $E_{2g}{}^1(\Gamma)$ and $A_{1g}(\Gamma)$ modes observed at 354.4 cm^{-1} and 418.9 cm^{-1}, respectively. Additional peaks corresponding to the 2LA(M)–$E_{2g}(\Gamma)$ and 2LA(M) modes are identified at 322.8 cm^{-1} and 349.4 cm^{-1}, respectively. Notably, a unique Raman peak associated with WS_2 nanotube structures, the $B_{1u}(\Gamma)$ mode, is also detected at 415.8 cm^{-1}, in agreement with previous studies.[43–45] The presence of the $B_{1u}(\Gamma)$ mode is attributed to the curvature-induced vibrational mode of the nanotube structure. Photoluminescence (PL) analysis (Fig. 6f) further corroborates WS_2 formation, revealing an exciton peak at 2.03 eV and a trion peak at 1.97 eV. These values are within the range of typically reported PL peak positions under similar low-power laser excitation conditions.[46] Transmission electron microscopy (TEM) analysis of as-grown nanostructures, transferred to a TEM grid (Fig. 6c), confirms that the nanowires consist of a solid tungsten oxide core coated with 1–3 WS_2 layers. Fig. S5 also includes a series of fast

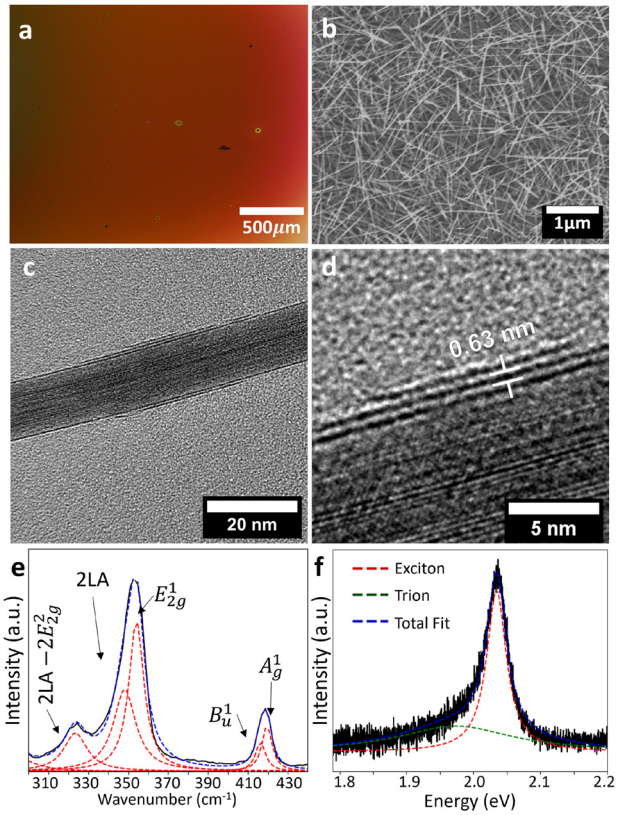

Fig. 6 (a) OM and (b) SEM images of the surface of a sample fabricated under the conditions: top substrate T = 722 °C, P = 0.02 mbar, with the average diameter of the sample $\bar{d}$ = 13 nm; (c) TEM image of a WS_2 nanotube with a WO_{3-x} core; (d) higher magnification image of (c) showing an interlayer distance of 6.3 Å, consistent with inter-plane spacing in WS_2 nanotubes; (e) Raman spectrum and fitted component curves measured at the centre of the sample, marked by a white-dashed circle, where peaks of 2LA(M)–$E_{2g}(\Gamma)$ are found at 322.8 cm^{-1}, the 2LA (M) mode at 349.4 cm^{-1}, $E_{2g}{}^1(\Gamma)$ mode at 354.4 cm^{-1}, $A_{1g}(\Gamma)$ mode at 418.9 cm^{-1}, and $B_{1u}(\Gamma)$ mode at 415.8 cm^{-1}; (f) PL spectrum and fitted component curves of the sample, with the exciton peak found at 2.03 eV and the trion peak at 1.97 eV. The size of the WO_3 precursor used is 1 × 1 cm^2.

Fourier transform (FFT) analyses and observed lattice spacings within the inner core corresponding to the WO_{3-x} phase.[11,15,17,19] The WS_2 outer layers exhibit an interlayer spacing of 0.63 nm, consistent with prior literature.[11] Additionally, the elemental distribution profiles shown in Fig. S6 present corresponding energy-dispersive X-ray spectroscopy (EDX) elemental maps for O, W, and S. Furthermore, fine WS_2 nanotubes with a WO_{3-x} core can also be grown on a sapphire substrate and a gold foil substrate (Fig. S7) under similar growth conditions, showing that our CSS method is versatile to various substrates.

2-Step process design: CSS-derived WO_{3-x} combined with sulfidation in a hot-wall CVD reactor

The use of hot-wall reactors in fabricating low-dimensional TMDC materials is dominant across the literature, particularly in connection with powder precursors.[47,48] Hence to connect and compare more closely, we explored a 2-step process flow by combining CSS-deposited W sub-oxide templates with subsequent sulfidation in a hot-wall CVD system. The WO_{3-x} precursor was fabricated under the same conditions as described in the previous section: a 1 mm × 1 mm square-patterned WO_3 film ($r \approx 1$ mm) was subjected to CSS at 760 °C for 10 minutes in an inert environment. The resulting WO_{3-x} structures were then transferred and sulphurised in a hot-wall CVD reactor using sulphur powder as the precursor at 650 °C for 1 h at atmospheric pressure (1 bar) with 200 sccm Ar carrier gas flow. A summary of growth conditions is given in Table S3.

OM imaging (Fig. S8) reveals a colour contrast similar to that observed in single-step sulfidation performed in a cold-wall CVD system. The central region (R < 0.5 mm) appears darker compared to that of the pre-sulfidation sample. Distinct WS_2 morphologies were observed across different regions of the substrate, correlating with the dominant WO_{3-x} phases present prior to sulfidation. As shown in Fig. 7b, regions initially dominated by bulky WO_{3-x} blocks underwent conversion to vertically oriented WS_2 flakes, forming a nanoflower-like morphology. In areas where WO_{3-x} nanorods and longer nanowhiskers were prevalent, hot-wall reactor sulfidation resulted in bundles of WS_2 nanowires (500–800 nm in length) extending from multi-layer WS_2 flakes (Fig. 7c). Conversely, in regions where smaller WO_{3-x} nanowhiskers were dominant, the resulting WS_2 structures consisted primarily of monolayer and bilayer WS_2 flakes with an average edge length of 3 μm (Fig. 7d).

Raman spectroscopy confirms the presence of multi-layer and bulk WS_2 in the regions corresponding to Fig. 7b and c. The measured peak separation between the $E_{2g}{}^1$ and $A_g{}^1$ modes is $\Delta\omega$ = 68.7 cm^{-1} and 67.8 cm^{-1}, respectively, consistent with thicker WS_2 layers. In contrast, the peak separation in Fig. 7d is $\Delta\omega$ = 64.7 cm^{-1}, characteristic of monolayer WS_2. These results align with previous Raman studies, which report a decrease in $\Delta\omega$ with reducing WS_2 layer thickness.[49,50] The PL spectra in Fig. 7f reveal a blue-shift in the excitonic peak from 1.93 eV in monolayer (ML) WS_2 (Fig. 7g) to 2.03 eV in both nanowire (NW) and nanoflower (NF) morphologies. At the same time the measured PL intensities for NF and NW morphologies are significantly lower than that for the ML. These results are consistent with previous literature on PL emission for WS_2 nanotubes and core–shell structures, showing a range of exciton energies depending *e.g.* on interlayer coupling, curvature, doping, dielectric environment, and excitation power.[16,46,51,52] The trion peaks at 1.87 eV in NW and NF, and at 1.85 eV in ML WS_2, suggest moderate doping in all three samples.[53] We emphasise that the observed PL arises exclusively from sulfidised WS_2 nanostructures; no detectable PL was found in non-sulfidised WO_{3-x} samples. The data demonstrate that the range of distinct WS_2 nanostructures accessible with our approach is similar to what has been previously reported in the literature for all furnace based synthesis.[15,21,54]

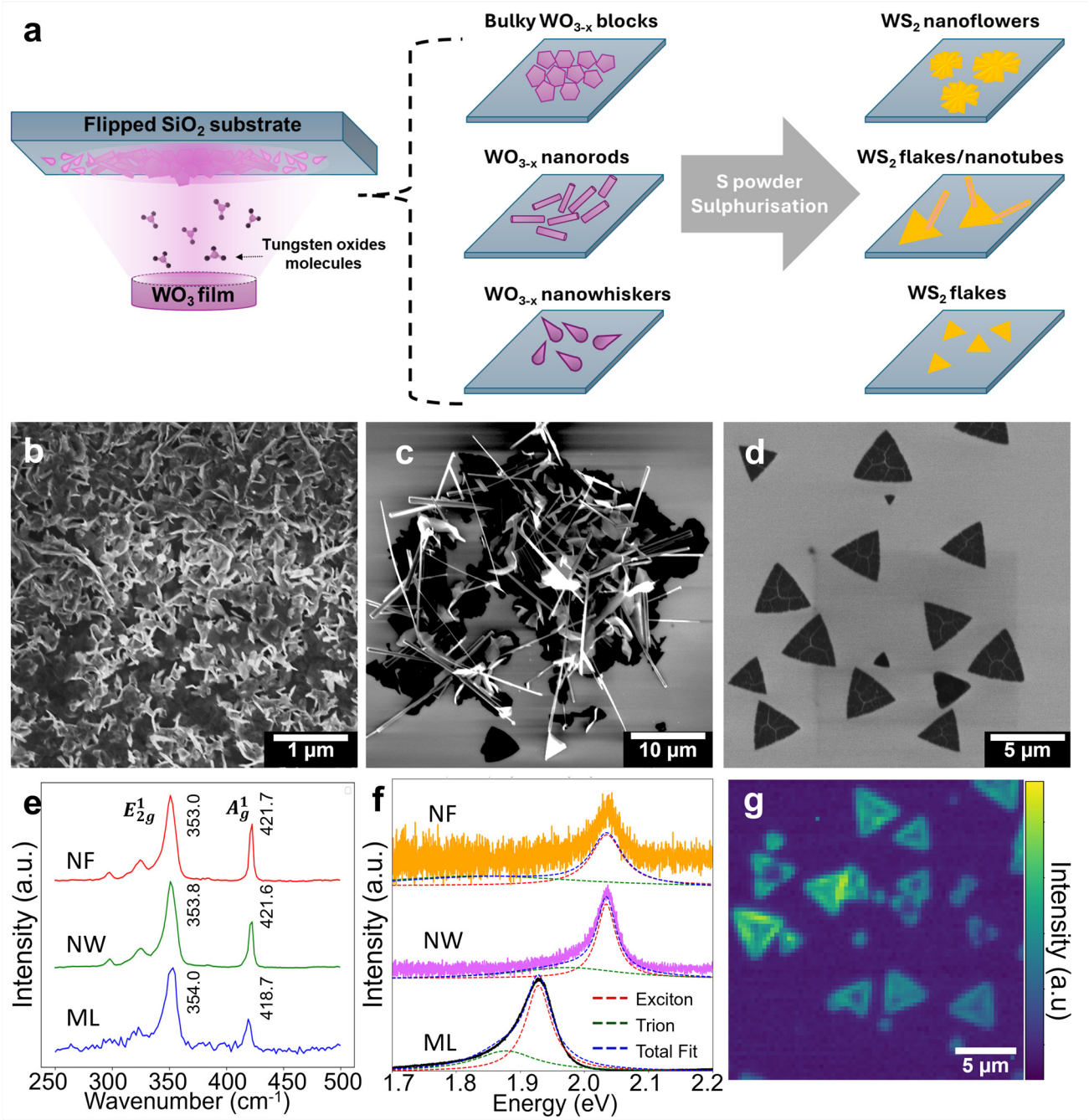

Fig. 7 (a) Schematic illustrating how different CSS-deposited WO_{3-x} phases lead to distinct WS_2 morphologies after extended sulfidation in a hot-wall CVD; (b) SEM image of WS_2 nanoflowers converted from bulky WO_{3-x} blocks; (c) SEM image of a mixed WS_2 nanowire-flake structure derived from WO_{3-x} nanorods; (d) SEM image of WS_2 monolayer flakes formed from WO_{3-x} nanowhiskers; (e) Raman spectra corresponding to the phases shown in (b–d), with resonance peaks labeled as E_{2g}^1 and A_g^1; (f) comparative PL spectra and fitted component curves of monolayer (ML) WS_2, WS_2–WS_{3-x} core–shell nanowires (NW), and WS_2 nanoflowers (NF). The ML sample exhibits an exciton peak at 1.93 eV and a trion peak at 1.85 eV, while both NW and NF samples show an exciton peak at 2.03 eV and a trion peak at 1.87 eV. All spectra are normalised for comparative visualisation; and (g) heatmap of integrated PL intensity between 1.8 and 2.0 eV for the WS_2 flake sample.

Discussion

W oxide morphology control with CSS flux

Our CSS "zone-maps" (Fig. 5) highlight that sublimation flux and substrate temperature are the key parameters to nano-structural control. The observed morphological range is consistent with the wide range of known W sub-oxide phases and morphologies.[17,31,35,39] The WO_3 structure is based on corner-sharing [WO_6] octahedra, whose atomic displacements and rotations can, depending on temperature, lead from monocli-

nic to tetragonal, orthorhombic or triclinic crystal symmetries. Upon reduction to W suboxides, the octahedra transition from corner-sharing to edge-sharing configurations, with a tendency to form crystallographic shear (CS) planes and Magneli phases.[17,27,55,56] This structural and reaction anisotropy results in the appearance of high-aspect ratio nanostructures and highly directional NW growth. Our XPS data for graded flux experiments (Fig. 2) show increasing W oxide reduction with increasing radial distance R, *i.e.* with lowering of the CSS flux. Tungsten trioxide sublimation is congruent, and under molecular flow conditions, the as-deposited W oxide is expected to have a stoichiometry close to that of WO_3, forming intermediate polymeric species such as W_3O_9, W_2O_6, and W_4O_{12}.[28–30] It is known, however, that the annealing of W oxides under vacuum leads to a release of oxygen.[31,35,39] We thus propose that structural control in our CSS process stems from the balance of deposition flux to the thermal loss of the oxygen/reduction rate of as-deposited W oxide on the substrate. For a given substrate temperature and thus fixed thermal reduction rate, a high sublimation flux (small R) results in a stoichiometry close to that of WO_3 or $W_{20}O_{58}$ and a related dense, bulky morphology. Conversely, for larger R, *i.e.* in the outer regions of the graded CSS deposition, the CSS flux is lower; hence the deposited W oxide is increasingly prone to thermal reduction. This leads to a transformation to sub-oxide phases such as $W_{18}O_{49}$ and nanowhiskers or nanorods becoming the dominant structural motif. The easy-to-control flux and rate balance in our CSS set-up thus enables us to efficiently control and access any of the known W sub-oxide phases and structures.

Structural changes of CSS deposited W oxides upon sulfidation

Our *operando* SEM data (Fig. 3) show significant structural changes upon sulfidation of CSS deposited W (sub)oxide templates as part of a 2-step process flow. It is well established that sulphur exposure leads to a surface reduction in W (sub) oxides.[57,58] An oxygen–sulphur exchange mechanism has been suggested, wherein sulphur atoms substitute oxygen at the corner positions of [WO_6] octahedra, leading to an increased degree of unsaturation of the metal cation due to the lower electronegativity of sulphur compared with that of oxygen.[59,60] The distinct morphologies for a 2-step process (Fig. 7) thus arise from a further reduction of the W (sub)oxide template of step 1 and deposition of WS_2 layers on the surface, both processes combined driving the structural transformation at step 2. We note that for our 2-step processes there is no supply of W oxide in step 2. Also the sulphur chemical potential is low for our DMDS exposures compared to S exposures in a furnace. For our DMDS-based processes and the relatively short exposures, we thus expect a limited surface coverage of maximum a few layers of WS_2, consistent with the first stage of previously reported "surface-inward" processes.[27] The rapid axial growth of the WO_{3-x}–WS_2 core–shell structure we observe by OSEM can be attributed to the small initial dimensions of the nanowhiskers (width < 20 nm, length < 200 nm), which facilitate efficient diffusion of tungsten suboxide species from the high-concentration core to the oxide-deficient tip. We observe that the axial growth only lasts for a short time (Fig. 3), which is consistent with the depletion of the WO_{3-x} core, leading to the exhaustion of the W suboxide supply necessary for continued axial growth. In contrast, bulk WO_{3-x} regions remain largely unchanged in the structure beyond this time frame, further supporting the role of precursor volatility in determining the final WS_2 morphology.

For the 2-step process, where we carried out sulfidation in a more S-rich furnace environment (Fig. 7), we observe a wider range of structural transformations in step 2. This range is consistent with previous literature in which both process steps were carried out in hot-walled furnaces,[15,54,61] with significantly longer process times required for step 1. CSS grown fine nanowhiskers (<200 nm in length) at step 1 undergo conversion into triangular monolayer WS_2 flakes (Fig. 7). The fine nanowhiskers thereby act as nucleation sites and W reservoirs for WS_2 flake growth. However, their small size limits the available W, restricting the formation of larger WS_2 domains. Longer WO_{3-x} nanowhiskers or nanorod-like phases (>500 nm in length) convert into WS_2 nanotubes and mesh-like structures. While nanowhiskers continue to serve as nucleation sites and W reservoirs for WS_2 flake growth on the SiO_2/Si substrate, their tendency to coalesce into clusters hinders in-plane expansion. Instead, under S-rich conditions, longer nanowhiskers undergo reduction and sulphur replacement *via* "surface-inward" mechanisms. Additionally, the previously indicated higher volatility of W_4O_{11} and W_2O_5 phases[14,62,63] can rationalise the extension of WS_2 flakes from nanotube tips resulting in a mixed WS_2 flake/nanotube mesh structure.[15] At regions where bulky WO_{3-x} facets with a higher W oxidation state are present, vertically aligned WS_2 nanoflowers become the dominant morphology. The less reduced WO_{3-x} bulky blocks require longer times for S-exchange and reduction; hence WO_xS_{2-x} intermediates form on the rough surfaces of the WO_{3-x} blocks.[57] Compared with fine nanowhiskers, the greater W content in these bulky blocks facilitates the growth of multilayer WS_2. Furthermore, compression and extrusion between several WS_2–WO_xS_{2-x} intermediate layers cause the WS_2 flakes to expand vertically.[42,54]

Single-step CSS process design

By additionally introducing a gaseous sulphur supply such as DMDS during W oxide sublimation, a 1-step CSS process flow can be implemented (Fig. 5 and 6). Compared to the 2-step process design, there will be a continuous supply of W oxide and a more complex kinetic interplay of the above discussed processes. Higher substrate temperatures ($T_{substrate}$) enhance both the oxide flux and the sulfidation rate. WS_2 flakes can rapidly grow out of the plane, suppressing the formation of W suboxide nanowhiskers necessary for WS_2 nanotube growth.[54] Consequently, nanoflower phases become dominant (Fig. 5). In contrast, at lower substrate temperatures the sublimation flux is compromised and the sulfidation rate is low; hence the deposits primarily consist of W suboxide nanowhiskers.[15]

Intermediate temperatures (~705 °C) lead to the formation of nanowhiskers and nanorods. Similar nanostructures have been achieved *via* hot-wall CVD, using WO_3 powder with sulphur vapour[15] or tungsten filaments with H_2O vapour in a tube furnace.[17,19] However, these approaches require significantly higher temperatures (>1000 °C). Notably, face-to-face substrate–precursor configurations in APCVD and hot-wall CVD methods result in minimal temperature gradients (ΔT), leading to high reflection fluxes (n_{counter}) of re-emitted WO_{3-x} from the substrate.[23] This suppresses nanowhisker formation. In contrast, our CSS setup exploits a larger ΔT, where the precursor temperature is approx. 20% higher than the substrate temperature, reducing reflection flux and enhancing net flux for efficient oxide nanowhisker and nanorod growth.

Conclusion

This study demonstrates the potential and efficacy of CSS in facilitating the controlled growth of WO_{3-x} and WS_2 nanostructures. By identifying and tuning the key parameters of deposition flux and substrate temperature, we achieved replication of the wide range of morphologies reported for much more cumbersome and inefficient hot-wall furnace growth, from WO_{3-x} nanowhiskers to WS_2 nanotubes, WS_2 2D layers and hybrid heterostructures. We highlighted the versatilty of the CSS approach by implementing sequential 2-step and combined 1-step process designs. For W (sub)oxide synthesis our CSS approach enables process times of less than 10 min, compared to previous hour long times. The CSS set-up is simple and warrants cleaner conditions, hence also enabling us to address the notoriously low reproducibility linked to nanostructural growth in CVD furnaces. Our work also highlights how the use of graded CSS flux profiles can be used for accelerated combinatorial process discovery and parameter optimisation. We showed how the as-identified conditions can be readily scaled up by increasing the lateral solid source dimensions. While we focussed on the W oxide/sulfide system, the demonstrated CSS approach is compatible with a wide range of material systems, and thus introduces an interesting, readily accessible alternative process path particularly to build on the numerous previous hot-wall furnace growth studies.

Experimental methods

Fabrication of a WO_3 thin film precursor

A uniform WO_3 thin film was deposited onto a Si substrate with native oxide using a HiTUS magnetron sputtering system. Initially, Ar gas was introduced to generate an Ar plasma, which was employed to clean the surface of the W target and sputter the film. Subsequently, high-purity oxygen gas was introduced during the deposition process to facilitate oxidation of the sputtered film. For the patterned WO_3 sample, a shadow mask with desirable pinhole size was used during sputtering to define the pattern. The film thickness was examined using an atomic force microscope (Asylum AFM) and determined to be 180 nm on average.

Fabrication of WO_{3-x} nanostructures and WS_2–WO_{3-x} heterostructured phases

SiO_2 (100 crystal plane, N-doped, 200 nm oxide layer) was cut to 10 mm × 10 mm size. The substrates were placed in acetone and subsequently in isopropanol alcohol (IPA) and sonic-cleaned for 5 minutes each, then dried by blowing N_2 gas and placed under a hotplate at 180 °C. The substrates are then activated by soft oxygen plasma (RIE, Manchester Instrument) for 10 minutes.

The WO_3 thin film precursor is placed on the graphite heating pad at the bottom of the sample holder. The clean SiO_2 substrate is placed facing downwards on top of the WO_3 thin film, separated by a sapphire chip spacer (thickness = 0.46 mm). The sample and sample holder are heated using an infrared high power laser (40–60 W), which heats up the graphite heating pad. The temperature is measured from the top of the substrate using a pyrometer that has been pre-calibrated with thermocouples. The chamber pressure is maintained at 0.02 mbar with a trace amount of Ar gas flow. For single-step fabrication of the WS_2–WO_{3-x} nanostructure, no Ar gas is used, and DMDS vapour is injected into the chamber from a canister containing liquid DMDS. After 10 minutes of heating, the laser power is switched off, and immediately the gas valve controlling the reaction gases is turned off. A plot of the heat ramp and gas ramp can be found in Fig. S1.

For extended sulfidation, a mixed WO_{3-x} nanostructure deposited on a SiO_2 substrate was placed at the center of a dual-zone tube furnace. The furnace temperature was raised to 650 °C and maintained for 1 hour at ambient pressure. During the reaction, 200 mg of sulphur powder was placed in the lower-temperature zone and heated to 180 °C. A 200 sccm Ar gas was used as a carrier gas. After the reaction, the furnace was allowed to cool naturally to room temperature.

In operando SEM characterisation

SEM images are taken in Zeiss Gemini 300 SEM. The electron voltage is generally kept at 5 kV. Both InLens and SE2 images are taken under various magnification ranges. An *in operando* SEM micro gas-injector is installed in a similar form to that in a previous study:[40] the gas precursor, stored externally to the SEM environment, is introduced into the chamber through a designated route consisting of a leak valve, bellow, and nozzle. To regulate the flow of precursors, leak valves situated on the manifold are controlled. This controlled introduction of precursors enables us to maintain a consistent flow during the experiments. A localized gas injection system is applied through a tapered quartz nozzle, with a tip diameter of approximately 10 μm. The nozzle is made from a micropipette puller. A WO_{3-x} nanowhisker-coated substrate is heated to 700 °C. A thermocouple is mounted on the stage to monitor the stage temperature.

Raman spectroscopy and PL measurement

A Renishaw Raman InVia microscope was used for both Raman spectroscopy and photoluminescence (PL) measurements of the deposited sample. A 532 nm laser with a low power density (0.06 mW cm^{-2}) was used to minimize peak shifts caused by laser-induced heating. The signal from the substrate (Si) was collected as a reference, subtracted to obtain the net intensity across different wavenumbers, and normalized by removing background signals. A Lorentzian model was used for Raman and PL peak fitting. For PL mapping, the integrated area of PL response under the spectral range of 1.8–2.0 eV was computed using Simpson's rule to provide quantitative distribution of the PL intensity.

X-ray photoelectron spectroscopy measurement

XPS analysis was performed using a Thermo NEXSA G2 XPS fitted with a monochromated Al Kα X-ray source (1486.7 eV), a spherical sector analyser, 3 multichannel resistive plates, and 128 channel delay line detectors. All data were recorded at 19.2 W and an X-ray beam size of 400 × 200 μm. Survey scans were recorded at a pass energy of 200 eV, and high-resolution scans recorded at a pass energy of 50 eV. Electronic charge neutralization was achieved using an ion source (Thermo Scientific FG-03): ion gun current = 150 μA and ion gun voltage = 40 V. All sample data were recorded at a pressure below 10–8 Torr and a room temperature of 294 K. Data were analysed using CasaXPS v2.3.26rev1.0N. Peaks were fit with a Shirley background prior to component analysis. Lineshapes of LA (1.53, 243) were used to fit components.

TEM and EDX characterisation

Transmission electron microscopy (TEM) images were obtained with a FEI TECNAI F20 transmission electron microscope equipped with a field emission gun and a GATAN Rio16 CMOS camera. For EDX analysis an EDX (EDAX Apollo XLTW SSD) detector was used. The TEM was operated at a 200 kV acceleration voltage. The sample was prepared on a copper holey carbon-coated grid (Plano, 200 mesh).

Author contributions

S. Hofmann conceived the project. H. Yu designed and conducted CSS-facilitated CVD growth and Raman and PL measurements. J. Yang conducted the *in operando* SEM experiment. B. Fickl and B. C. Bayer conducted and interpreted TEM and EDX measurements. S. Guan performed XPS measurements. O. J. Burton advised on modelling of flux and design of the CSS set-up. G. Wyatt-Moon prepared WO_3 thin film precursors, supervised by A. Flewitt. S. Hofmann supervised the project. H. Yu and S. Hofmann wrote the manuscript.

Conflicts of interest

There are no conflicts of interest to declare.

Data availability

The data supporting this article have been included as part of the SI.

Supplementary information is available, providing OSEM video, additional characterisation data by SEM, TEM, OM, Raman and PL, as well as further analysis and summary tables of CSS process conditions. See DOI: **https://doi.org/10.1039/d5nr01458a**.

Acknowledgements

This work was supported by EPSRC (EP/T001038/1, EP/P005152/1). J. Y. acknowledges funding from EPSRC CDT in Nanoscience and Nanotechnology (EP/L015978/1) and Cambridge Display Technology Ltd. We acknowledge the help of Jake Meeth with calibrating the HiTUS magnetron sputtering system and also acknowledge the use of facilities at the University Service Centre for Transmission Electron Microscopy (USTEM) of the TU Wien, Austria.

References

1 S. Piskunov, O. Lisovski, Y. F. Zhukovskii, P. N. D'Yachkov, R. A. Evarestov, S. Kenmoe and E. Spohr, *ACS Omega*, 2019, **4**, 1434–1442.
2 Y. J. Zhang, T. Ideue, M. Onga, F. Qin, R. Suzuki, A. Zak, R. Tenne, J. H. Smet and Y. Iwasa, *Nature*, 2019, **570**, 349–353.
3 K. R. Keller, R. Rojas-Aedo, H. Zhang, P. Schweizer, J. Allerbeck, D. Brida, D. Jariwala and N. Maccaferri, *ACS Photonics*, 2022, **9**, 2683–2690.
4 Y. Divon, R. Levi, J. Garel, D. Golberg, R. Tenne, A. Ya'akobovitz and E. Joselevich, *Nano Lett.*, 2017, **17**, 28–35.
5 F. Qin, W. Shi, T. Ideue, M. Yoshida, A. Zak, R. Tenne, T. Kikitsu, D. Inoue, D. Hashizume and Y. Iwasa, *Nat. Commun.*, 2017, **8**, 14465.
6 H. Xia, X. Chen, S. Luo, F. Qin, A. Idelevich, S. Ghosh, T. Ideue, Y. Iwasa, A. Zak, R. Tenne, Z. Chen, W.-T. Liu and S. Wu, *Nano Lett.*, 2021, **21**, 4937–4943.
7 N. Briggs, S. Subramanian, Z. Lin, X. Li, X. Zhang, K. Zhang, K. Xiao, D. Geohegan, R. Wallace, L.-Q. Chen, M. Terrones, A. Ebrahimi, S. Das, J. Redwing, C. Hinkle, K. Momeni, A. Van Duin, V. Crespi, S. Kar and J. A. Robinson, *2D Mater.*, 2019, **6**, 022001.
8 International Roadmap for Devices and Systems (IRDSTM) 2022 Edition: Beyond CMOS and Emerging Research Materials, 2022, **https://irds.ieee.org/images/files/pdf/2022/2022IRDS_BC.pdf**.
9 R. Yadav, S. Poudyal, R. Rajarapu, B. Biswal, P. K. Barman, S. Kasiviswanathan, K. S. Novoselov and A. Misra, *Small*, 2024, **20**, 2309163.
10 W. K. Hsu, B. H. Chang, Y. Q. Zhu, W. Q. Han, H. Terrones, M. Terrones, N. Grobert, A. K. Cheetham, H. W. Kroto and

D. R. M. Walton, *J. Am. Chem. Soc.*, 2000, **122**, 10155–10158.
11 H. A. Therese, J. Li, U. Kolb and W. Tremel, *Solid State Sci.*, 2005, **7**, 67–72.
12 L. Yadgarov and R. Tenne, *Small*, 2024, 2400503.
13 Y. Liu, S. Zhang, J. He, Z. M. Wang and Z. Liu, *Nano-Micro Lett.*, 2019, **11**, 13.
14 A. Margolin, R. Rosentsveig, A. Albu-Yaron, R. Popovitz-Biro and R. Tenne, *J. Mater. Chem.*, 2004, **14**, 617.
15 Z. Liu, A. W. A. Murphy, C. Kuppe, D. C. Hooper, V. K. Valev and A. Ilie, *ACS Nano*, 2019, **13**, 3896–3909.
16 M. A. Rahman, Y. Yomogida, A. Ahad, K. Ueji, M. Nagano, A. Ihara, H. Nishidome, M. Omoto, S. Saito, Y. Miyata, Y. Gao, S. Okada and K. Yanagi, *Sci. Rep.*, 2023, **13**, 16959.
17 A. Rothschild, J. Sloan and R. Tenne, *J. Am. Chem. Soc.*, 2000, **122**, 5169–5179.
18 S. Sun, Z. Zou and G. Min, *Mater. Chem. Phys.*, 2009, **114**, 884–888.
19 A. Zak, L. Sallacan-Ecker, A. Margolin, Y. Feldman, R. Popovitz-Biro, A. Albu-Yaron, M. Genut and R. Tenne, *Fullerenes, Nanotubes Carbon Nanostruct.*, 2010, **19**, 18–26.
20 G. A. Asres, A. Dombovari, T. Sipola, R. Puskás, A. Kukovecz, Z. Kónya, A. Popov, J.-F. Lin, G. S. Lorite, M. Mohl, G. Toth, A. Lloyd Spetz and K. Kordas, *Sci. Rep.*, 2016, **6**, 25610.
21 M. O'Brien, N. McEvoy, T. Hallam, H.-Y. Kim, N. C. Berner, D. Hanlon, K. Lee, J. N. Coleman and G. S. Duesberg, *Sci. Rep.*, 2014, **4**, 7374.
22 T. C. Anthony, A. L. Fahrenbruch and R. H. Bube, *J. Vac. Sci. Technol., A*, 1984, **2**, 1296–1302.
23 J. L. Cruz-Campa and D. Zubia, *Sol. Energy Mater. Sol. Cells*, 2009, **93**, 15–18.
24 O. J. Burton, F. C.-P. Massabuau, V.-P. Veigang-Radulescu, B. Brennan, A. J. Pollard and S. Hofmann, *ACS Nano*, 2020, **14**, 13593–13601.
25 O. J. Burton and S. Hofmann, *APL Mater.*, 2024, **12**, 081106.
26 O. d. Melo, L. García-Pelayo, Y. González, O. Concepción, M. Manso-Silván, R. López-Nebreda, J. L. Pau, J. C. González, A. Climent-Font and V. Torres-Costa, *J. Mater. Chem. C*, 2018, **6**, 6799–6807.
27 V. Kundrát, L. Novák, K. Bukvišová, J. Zálešák, E. Kolíbalová, R. Rosentsveig, M. Sreedhara, H. Shalom, L. Yadgarov, A. Zak, M. Kolíbal and R. Tenne, *ACS Nano*, 2024, **18**, 12284–12294.
28 J. Berkowitz, W. A. Chupka and M. G. Inghram, *J. Chem. Phys.*, 1957, **27**, 85–86.
29 K. N. Marushkin, A. S. Alikhanyan, J. H. Greenberg, V. B. Lazarev, V. A. Malyusov, O. N. Rozanova, B. T. Melekh and V. I. Gorgoraki, *J. Chem. Thermodyn.*, 1985, **17**, 245–253.
30 R. J. Ackermann and E. G. Rauh, *J. Phys. Chem.*, 1963, **67**, 2596–2601.
31 K. Bange, *Sol. Energy Mater. Sol. Cells*, 1999, **58**, 1–131.
32 J. Safarian and T. A. Engh, *Metall. Mater. Trans. A*, 2013, **44**, 747–753.
33 G. Meyer, J. F. Oosterom and J. L. de Roo, *Recl. Trav. Chim. Pays-Bas*, 1959, **78**, 412–416.
34 T. Millner and J. Neugebauer, *Nature*, 1949, **163**, 601–602.
35 V. K. Sarin, *J. Mater. Sci.*, 1975, **10**, 593–598.
36 M. Weil and W.-D. Schubert, *International Tungsten Industry Association*, 2013, **4**, 1–12.
37 R. J. D. Tilley, *Colour and the optical properties of materials*, John Wiley & Sons, Inc., Hoboken, NJ, 3rd edn, 2020.
38 F. Y. Xie, L. Gong, X. Liu, Y. T. Tao, W. H. Zhang, S. H. Chen, H. Meng and J. Chen, *J. Electron Spectrosc. Relat. Phenom.*, 2012, **185**, 112–118.
39 S. Santucci, L. Lozzi, E. Maccallini, M. Passacantando, L. Ottaviano and C. Cantalini, *J. Vac. Sci. Technol., A*, 2001, **19**, 1467–1473.
40 J. Yang, Y. Fan, R. Mizuta, M. Rimmer, J. Donoghue, S. Guan, S. J. Haigh and S. Hofmann, *Chem. Mater.*, 2025, **37**, 989–1000.
41 M. Srinivaas, C.-Y. Wu, J.-G. Duh and J. M. Wu, *ACS Sustainable Chem. Eng.*, 2019, **7**, 10363–10370.
42 A. Prabakaran, F. Dillon, J. Melbourne, L. Jones, R. J. Nicholls, P. Holdway, J. Britton, A. A. Koos, A. Crossley, P. D. Nellist and N. Grobert, *Chem. Commun.*, 2014, **50**, 12360–12362.
43 M. Viršek, A. Jesih, I. Milošević, M. Damnjanović and M. Remškar, *Surf. Sci.*, 2007, **601**, 2868–2872.
44 M. Krause, M. Viršek, M. Remškar, N. Salacan, N. Fleischer, L. Chen, P. Hatto, A. Kolitsch and W. Müller, *ChemPhysChem*, 2009, **10**, 2221–2225.
45 M. Staiger, P. Rafailov, K. Gartsman, H. Telg, M. Krause, G. Radovsky, A. Zak and C. Thomsen, *Phys. Rev. B:Condens. Matter Mater. Phys.*, 2012, **86**, 165423.
46 V. Kundrát, R. Rosentsveig, K. Bukvišová, D. Citterberg, M. Kolíbal, S. Keren, I. Pinkas, O. Yaffe, A. Zak and R. Tenne, *Nano Lett.*, 2023, **23**, 10259–10266.
47 L. Tang, J. Tan, H. Nong, B. Liu and H.-M. Cheng, *Acc. Mater. Res.*, 2020, **2021**, 36–47.
48 B. Qin, M. Z. Saeed, Q. Li, M. Zhu, Y. Feng, Z. Zhou, J. Fang, M. Hossain, Z. Zhang, Y. Zhou, Y. Huangfu, R. Song, J. Tang, B. Li, J. Liu, D. Wang, K. He, H. Zhang, R. Wu, B. Zhao, J. Li, L. Liao, Z. Wei, B. Li, X. Duan and X. Duan, *Nat. Commun.*, 2023, **14**, 304.
49 A. Berkdemir, H. R. Gutiérrez, A. R. Botello-Méndez, N. Perea-López, A. L. Elías, C.-I. Chia, B. Wang, V. H. Crespi, F. López-Urías, J.-C. Charlier, H. Terrones and M. Terrones, *Sci. Rep.*, 2013, **3**, 1755.
50 H. Zeng, G.-B. Liu, J. Dai, Y. Yan, B. Zhu, R. He, L. Xie, S. Xu, X. Chen, W. Yao and X. Cui, *Sci. Rep.*, 2013, **3**, 1608.
51 Q. An, W. Xiong, F. Hu, Y. Yu, P. Lv, S. Hu, X. Gan, X. He, J. Zhao and S. Yuan, *Nat. Mater.*, 2024, **23**, 347–355.
52 Q. Cui, Z. Luo, Q. Cui, W. Zhu, H. Shou, C. Wu, Z. Liu, Y. Lin, P. Zhang, S. Wei, H. Yang, S. Chen, A. Pan and L. Song, *Adv. Funct. Mater.*, 2021, **31**, 2105339.
53 A. O. A. Tanoh, J. Alexander-Webber, J. Xiao, G. Delport, C. A. Williams, H. Bretscher, N. Gauriot, J. Allardice, R. Pandya, Y. Fan, Z. Li, S. Vignolini, S. D. Stranks, S. Hofmann and A. Rao, *Nano Lett.*, 2019, **19**, 6299–6307.

54 E. Hossain, A. A. Rahman, R. D. Bapat, J. B. Parmar, A. P. Shah, A. Arora, R. Bratschitsch and A. Bhattacharya, *Nanoscale*, 2018, **10**, 16683–16691.
55 M. Kolíbal, K. Bukvišová, L. Kachtík, A. Zak, L. Novák and T. Šikola, *J. Phys. Chem. C*, 2019, **123**, 9552–9559.
56 Z. Zhang, Y. Wang, H. Li, W. Yuan, X. Zhang, C. Sun and Z. Zhang, *ACS Nano*, 2016, **10**, 763–769.
57 A. J. van der Vlies, G. Kishan, J. W. Niemantsverdriet, R. Prins and T. Weber, *J. Phys. Chem. B*, 2002, **106**, 3449–3457.
58 F. E. Massoth and D. L. Bidlack, *J. Catal.*, 1970, **16**, 303–315.
59 Y. Feldman, V. Lyakhovitskaya and R. Tenne, *J. Am. Chem. Soc.*, 1998, **120**, 4176–4183.
60 Y. Rong, Y. Fan, A. Leen Koh, A. W. Robertson, K. He, S. Wang, H. Tan, R. Sinclair and J. H. Warner, *Nanoscale*, 2014, **6**, 12096–12103.
61 J. Yan, Y. Huang, Z. Cao and Y. An, *Vacuum*, 2023, **208**, 111725.
62 B. Wang, W.-J. Chen, B.-C. Zhao, Y.-F. Zhang and X. Huang, *J. Phys. Chem. A*, 2010, **114**, 1964–1972.
63 P. Chithaiah, S. Ghosh, A. Idelevich, L. Rovinsky, T. Livneh and A. Zak, *ACS Nano*, 2020, **14**, 3004–3016.